Linear and nonlinear coupling between transverse modes of a nanomechanical resonator

P. A. Truitt, J. B. Hertzberg, E. Altunkaya, and K. C. Schwab

Citation: Journal of Applied Physics **114**, 114307 (2013); doi: 10.1063/1.4821273
View online: http://dx.doi.org/10.1063/1.4821273
View Table of Contents: http://scitation.aip.org/content/aip/journal/jap/114/11?ver=pdfcov
Published by the AIP Publishing

Linear and nonlinear coupling between transverse modes of a nanomechanical resonator

P. A. Truitt,[1,a] J. B. Hertzberg,[2] E. Altunkaya,[3] and K. C. Schwab[4]
[1]*Department of Mathematical Sciences, Montclair State University, Montclair, New Jersey 07043, USA*
[2]*Joint Quantum Institute and Department of Physics, University of Maryland, College Park, Maryland 20742, USA*
[3]*Montclair High School, Montclair, New Jersey 07042, USA*
[4]*Applied Physics, California Institute of Technology, Pasedena, California 91125, USA*

(Received 5 May 2013; accepted 31 August 2013; published online 18 September 2013)

We measure both the linear and nonlinear coupling between transverse modes in a nanomechanical resonator. The nonlinear coupling is due to the displacement dependent tension of the resonator and leads to a frequency shift ("pulling") of each mode proportional to the square of the orthogonal mode's displacement amplitude. The linear coupling is apparent as an avoided crossing of the resonant frequencies that occurs when one electrostatically tunes the modes into degeneracy via a nearby DC gate. We consider the possibility that the linear coupling results from an electrostatic interaction and find that this effect can only partially explain the magnitude of the observed coupling. By measuring the coupled amplitudes magnetomotively at various angles to the applied field, we find that as the modes are tuned through the degeneracy point, they remain linearly polarized, while their planes of vibration rotate by 90°. © *2013 AIP Publishing LLC*. [http://dx.doi.org/10.1063/1.4821273]

I. INTRODUCTION

Due to their small masses, high operating frequencies, and high quality factors, nanoelectromechanical systems (NEMS) have attracted interest for use in areas such as ultrasensitive mass sensing,[1,2] force microscopy,[3,4] and RF signal processing.[5,6] Recently, coupling between mechanical modes in these systems has become a topic of interest.[7–12] Such mode couplings can be important to NEMS applications as they can influence the resonator parameter that is being exploited.

For instance, one can tune the resonance frequency and quality factor of one mechanical mode through a nonlinear coupling to a second mode.[13,14] Nonlinear interaction between modes has also been proposed as a way to probe the energy eigenstate of a resonator.[15,16] Such a proposal is a mechanical analog to quantum nondemolition strategies, which employ the optical Kerr effect to detect the quantization of the electromagnetic field.[17]

This nonlinear coupling is realized by the stretching of the resonator during oscillation. For instance, in a clamped beam type resonator, the tension along the axis is given by[18]

$$T(x,y) = AE\frac{\Delta\ell(x,y)}{\ell}, \\ = \frac{AE}{2\ell}\int_{-\ell/2}^{\ell/2}\left(\left(\frac{\partial x}{\partial z}\right)^2 + \left(\frac{\partial y}{\partial z}\right)^2\right)\mathrm{d}z, \qquad (1)$$

where A is the cross sectional area, E is the Young's modulus, ℓ is the beam's axial length along z, and x and y are transverse displacements in and out of the plane of the substrate, respectively (see inset to Fig. 1). This dependence of the tension on the amplitude of transverse motion results in the familiar Duffing response, where the peak amplitude frequency of the mode shifts upward with increasing drive amplitude. The same mechanism will result in a nonlinear coupling between two modes, as each mode will be affected by the tension resulting from the other mode's displacement. This effect has previously been demonstrated between different order modes oscillating in the same plane,[14] whereas the coupling we explore in this work is between fundamental modes oscillating in orthogonal directions.

In addition to nonlinear coupling, many systems also exhibit a linear coupling between modes. This type of coupling has been applied to mass sensing,[19] signal amplification,[20] and synchronization of arrays of resonators.[21]

Linear coupling can be of an elastic nature when two or more resonator modes share a common support.[7,19] It can also occur as a consequence of the electromagnetic environment that the resonator is embedded in, as when a resonator is being actuated and detected capacitively. This coupling can be observed between two resonators in proximity, mediated through the capacitance between them,[20] as well as between orthogonal modes of a single resonator interacting with one or more nearby gate electrodes, as demonstrated recently.[12] To understand the latter, consider a typical capacitive detection scheme,[22] where a resonator is capacitively coupled to a nearby gate electrode. In order to achieve sensitive detection, a DC bias (V_g) is applied between the gate and the beam, which gives a force on the resonator

$$\boldsymbol{f} = -\nabla U = \frac{V_g^2}{2}\nabla C, \qquad (2)$$

where the total energy in the system, U, is comprised of the energy stored in the electric field between the beam and gate as well as the energy in the voltage supply that maintains the constant voltage V_g between them. Expanding the capacitance

[a]Electronic mail: truittp@mail.montclair.edu

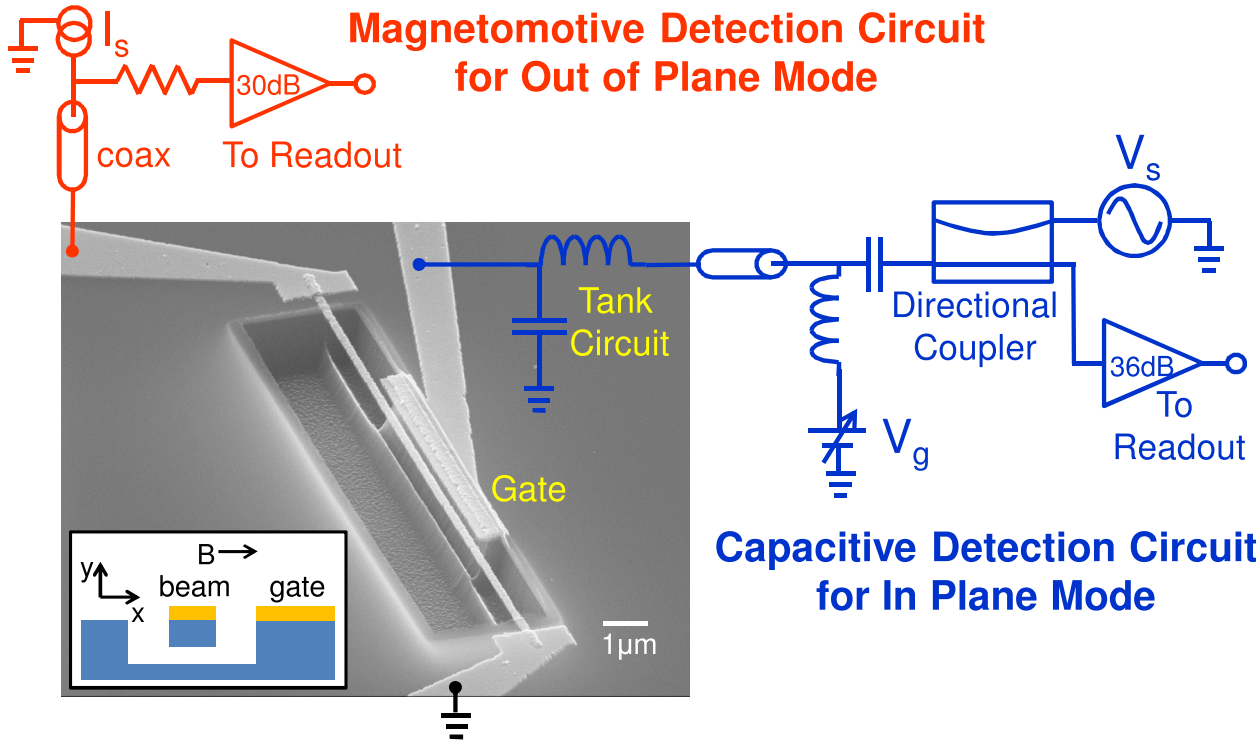

FIG. 1. SEM of a typical device along with measurement circuits. The amplifier used for magnetomotive detection (CLC425) has a 3 kΩ input impedance (DC resistance of beam ≃1.6 kΩ), while a tank circuit ($L_t = 62\,\mu$H, $C_t = 5.4$ pF, $R_t = 120\,\Omega$) is used to match the impedance of the beam to a 50 Ω amplifier (Miteq) for capacitive detection at approximately 8.5 MHz. The inset schematic shows a cross section of the device and the coordinate system used: the in-plane mode and magnetic field are along x, with the transverse out-of-plane mode along y.

per unit length C in both displacements x and y, we find an electrostatic force per unit length in the in-plane direction (x mode) to be

$$f_x = \frac{V_g^2}{2}\left(\frac{\partial C}{\partial x} + \frac{\partial^2 C}{\partial x^2}x + \frac{\partial^2 C}{\partial x \partial y}y\right). \tag{3}$$

The first term above leads to a static shift in the beam's equilibrium position. The second term, which is a linear function of x, modifies the linear restoring force on the beam and gives a voltage dependent contribution to the spring constant.[23] The last term produces a force in the x direction due to a displacement in the y direction, providing a linear coupling between transverse modes of oscillation. Electrostatic forces for the out-of-plane displacement (y mode) follow the same form.

In this work, we consider both linear and nonlinear coupling between the two fundamental transverse modes of a single resonator. Combining both couplings, the dynamics of two modes can be described by two coupled equations of motion

$$F_x = M\ddot{X} + D_x\dot{X} + K_xX + K_{xy}Y + K_T(X^3 + Y^2X), \tag{4a}$$

$$F_y = M\ddot{Y} + D_y\dot{Y} + K_yY + K_{yx}X + K_T(Y^3 + X^2Y). \tag{4b}$$

Uppercase X and Y are used to represent the time dependent amplitudes of the fundamental transverse modes, $X = X_0\cos(\omega_x t)$ and $Y = Y_0\cos(\omega_y t)$, as opposed to the z-dependent transverse displacements, x, y. Coefficients appearing in Eq. (4) are effective values including the effect of the mode shape of the beam. M is the effective mass of the beam and D_x and D_y are the dissipation constants. K_x and K_y are the spring constants including the electrostatic contribution, $K_{xy} = K_{yx}$ are the linear coupling from the electrostatics, and K_T is the nonlinear spring constant due to tension. In what follows, we have chosen to normalize X and Y by setting the effective length of the beam equal to the actual length, which defines X and Y as the average displacements over the length of the beam, respectively. A more detailed explanation of Eq. (4) and the coefficients therein can be found in the appendix.

II. SETUP

The structures used in this study are clamped-clamped beams fabricated using standard electron-beam lithography (EBL), e-beam evaporation, and reactive ion etching (RIE).[24–26] We began with a substrate consisting of 500 μm thick p-type silicon coated with 100 nm of amorphous, low-stress, LPCVD Si_3N_4. We used EBL and e-beam evaporation to define an array of beam and gate electrodes with a bilayer of 30 nm Al + 5 nm Au. The beam/gate patterns were connected to bond-pads by Ti + Au traces defined in an additional EBL step. The metallic coating on the beam and gate is used for transducing the resonator motion and also served as a mask during the etching steps described next.

The beams were freely suspended by using a two-step undercutting RIE scheme, as follows: Over the beam, we defined a window of length 16.2 μm in a PMMA mask using EBL. We then used an anisotropic RIE recipe (175 W, 40 mT, 18 ccm CHF_3, 2 ccm O_2) to remove the Si_3N_4 within the window. This etch was immediately followed by an isotropic RIE

recipe (75 W, 40 mT, 20 ccm SF_6) to etch the silicon beneath the beam and leave a freestanding Si_3N_4 (plus metal) beam. This technique produces beams of well-defined length and width but leads to uncertainty in the thickness of the metal coating: the plasma etch thins the metal on top of the beam. In addition, an unknown residue of silicon can be expected on the underside of the beam, which is impossible to view with the scanning electron micrograph (SEM). Using other test samples, we estimate that about 25 ± 5 nm of Al is left on the beam.

The dimensions of the beam measured in this study are as follows: length $\ell = 16.2 \pm 0.01\,\mu$m, width in the plane of the substrate $w = 220 \pm 10$ nm, and thickness $h = 125 \pm 10$ nm. A gate electrode of length 8.75 μm is positioned 165 ± 10 nm away. For the given dimensions, we calculate a resonator mass of 1.3 picograms. Fig. 1 shows an SEM image of a device similar to the ones measured.

We placed each device in a high vacuum chamber ($<10^{-5}$ Torr) in thermal contact with a 4.2 K liquid helium bath. A carbon-glass thermometer attached to the gold-plated, copper sample package indicated that the sample temperature was below 5 K. We grounded one end of the beam at the sample package, with the other end of the beam and the gate connected to room temperature electronics through semi-rigid coaxial cables. A magnetic field was applied perpendicular to the beam axis and in the plane of the sample. Fig. 1 includes schematics of both detection circuits. By fitting the frequency response of each detection circuit using the appropriate electromechanical impedance model for the resonator,[22,27] we determined the magnetic field strength at the sample, and also determined an estimate of the total beam-gate capacitance, $C_{bg} = 46$ aF.

III. RESULTS AND DISCUSSION

A. Nonlinear coupling

Before looking at the coupling between the two modes, we first measured their individual spring constants by recording the frequency response of the two modes at low gate bias and low driving amplitude (under 1 nm displacement), such that the nonlinear and coupling terms in Eq. (4) can be ignored. Lorentzian fits give resonant frequencies of $f_{0,x} = 8.74$ MHz and $f_{0,y} = 8.42$ MHz with quality factors $Q_x = 2.50 \cdot 10^4$, $Q_y = 3.30 \cdot 10^4$. With such high quality factors, the natural frequencies are related to the spring constants through $K = M(2\pi f_0)^2$. Using this relationship, we find our experimentally measured spring constants to be $K_x^{ex} = 5.7 \pm 0.5$ N/m and $K_y^{ex} = 5.3 \pm 0.5$ N/m. Assuming a simple rectangular cross section for the beam, theoretical values (see appendix) were determined to be $K_x^{th} = 4.8$ N/m and $K_y^{th} = 1.2$ N/m.

The measured K_x for the in-plane mode, is seen to have good agreement with theory (within 20%), while the out-of-plane value is observed to be 4.5 times larger than our prediction. We believe that the most likely explanation for this discrepancy is the possibility of residual silicon attached under the beam after etching. Since the moment of inertia is proportional to the cube of the thickness in the direction of motion, such an addition to the cross section of the beam would have a substantial effect on the out-of-plane stiffness without affecting the in-plane value. In fact, we find that assuming a 100 nm deep triangle of silicon is left under and attached to the beam after etching gives $K_x^{th} = 4.7$ N/m and $K_y^{th} = 2.7$ N/m, thus significantly improving the agreement between theory and experiment for the out-of-plane mode, while not significantly affecting the in-plane agreement.

Next, we measured the nonlinear response and nonlinear mode coupling. By monitoring the frequency of each mode as its amplitude was changed, we determined the mode's Duffing response behavior at amplitudes well below the critical point. By monitoring each mode's frequency as the amplitude of the orthogonal mode was changed, we determined the nonlinear-coupling or "frequency pulling" behavior. During all four sets of measurements, we set the magnetic field and gate voltage to 0.38 T and 2 V, respectively. While at high DC voltages, the static deflection of the resonator toward the gate can introduce an additional quadratic nonlinearity,[23] we estimate that the static deflection generated here is less than 0.3 nm and produces a negligible correction to the nonlinear response. The out-of-plane mode was driven and detected using the magnetomotive method, while the in-plane mode was driven and detected capacitively. Frequencies were determined by Lorentzian fits, except for the measurement of frequency pulling of the in-plane mode by the out-of-plane mode, during which the frequency of the in-plane mode was monitored by a phase locked loop. The results are shown in Fig. 2. We note that if the orthogonal mode is driven a few linewidths off resonance, the "pulling" effect disappears—which demonstrates that heating (which might also be expected to produce a quadratic frequency shift with increasing drive amplitude due to the difference in thermal expansion coefficients of Si and Si_3N_4) is not the origin of the "pulling" effect.

For low oscillation amplitudes, the beam is in the weakly nonlinear regime and one can use a perturbative technique such as the Poincaré-Lindstedt method[28] to find an expression for the mode frequencies. Assuming negligible damping and ignoring the capacitive terms that are small at low gate bias, then to first order in $(K_T/K_x)X_0^2$ and $(K_T/K_y)Y_0^2$, we find

$$\omega_x = \omega_{0,x}\left(1 + \frac{3}{8}\frac{K_T}{K_x}X_0^2 + \frac{1}{4}\frac{K_T}{K_x}Y_0^2\right), \tag{5a}$$

$$\omega_y = \omega_{0,y}\left(1 + \frac{3}{8}\frac{K_T}{K_y}Y_0^2 + \frac{1}{4}\frac{K_T}{K_y}X_0^2\right). \tag{5b}$$

The second term in each equation gives the quadratic dependence of frequency on amplitude characteristic of a weakly driven Duffing oscillator. For the last term in each equation, we used the time average displacement of the orthogonal mode. This procedure works given that the two mode frequencies are separated by many linewidths. For degenerate eigenfrequencies, parametric oscillations due to the resonator tension varying at $2\omega_0$ would have to be taken into account, an effect not studied here. The quadratic relationship of frequency on oscillation amplitude of either mode is clearly seen in Fig. 2. According to Eqs. (5a) and (5b), the Duffing-type frequency shift of a mode due to its own amplitude should be 1.5 times larger than the frequency pulling due to the

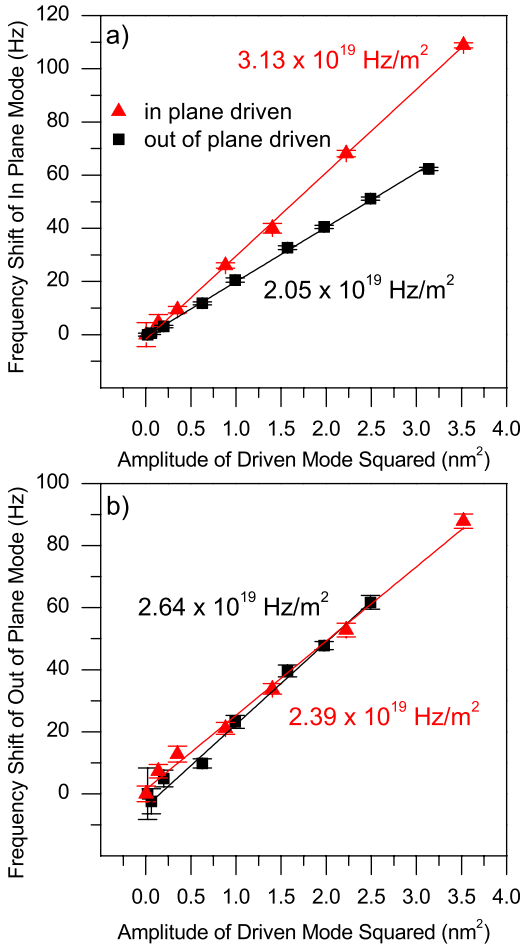

FIG. 2. Measured frequency shift of the (a) in-plane mode, measured using capacitive detection (using $V_g = 2\,\mathrm{V}$), and (b) out-of-plane mode, measured using magnetomotive detection (using $B = 0.38\,\mathrm{T}$), plotted against driven amplitudes. Triangular data points indicate that the in-plane mode is being driven, while squares indicate an out-of-plane drive. Lines are linear fits to the data. To determine resonator displacements, the signal measured by each detection circuit was fit to determine the gate capacitance and magnetic field, which determines the forces on the beam. The amplitudes of the beam were then calculated as $X_0 = F_x Q_x / K_x$ and $Y_0 = F_y Q_y / K_y$.

amplitude of the orthogonal mode. In Fig. 2, this relationship holds for the in-plane mode, which exhibits a ratio of 1.53. For the out-of-plane mode, however, the measured frequency shifts are nearly equal, with a ratio of 1.1.

The reason for the discrepancy between theory and experiment in the frequency shifts of the out-of-plane mode is not clear. It may indicate that K_T is not the same for the four nonlinear terms in Eq. (4). Equal nonlinear spring constants are a result of assuming that the two modes share the same mode shape, which appears reasonable in that they are both oscillations of a clamped-clamped beam in its lowest vibrational mode. However, it is possible that the out-of-plane mode has a slightly longer effective length due to the isotropic etch leaving a thin ledge of Si_3N_4 at the edge of the etch window that is able to flex in the out-of-plane direction along with the beam. The perimeter of this undercut can be seen as a bright line around the etch window in Fig. 1. From the SEM image, we estimate that the out-of-plane mode may be $0.4\,\mu\mathrm{m}$ longer than the in-plane mode. This difference raises the expected ratio of Duffing and pulling slopes for the in-plane mode to 1.54, thus improving the already good agreement with experiment in that case, and lowers the expected ratio for the out-of-plane mode to 1.46, which is a very small improvement. Another assumption implicit in our choice of mode shape is that the beam dynamics are dominated by the stiffness of the beam, and thus we ignored any residual tensile stress, σ, present in the Si_3N_4. The relative importance of these terms can be quantified through the ratio $R = \sigma A \ell^2 / 12EI$. For the LPCVD Si_3N_4 used, $E \simeq 300\,\mathrm{GPa}$ and σ is on the order of MPa, resulting in R ranging from about 0.1 to 1. Even in this range, using the zero stress mode shapes is expected to be a good approximation. For instance, we estimate the effect of residual stress on the mode natural frequencies to be limited to about 10%. However, because the bending moment, I, is about three times smaller for the out-of-plane mode than the in-plane mode, its mode shape will be affected more by the residual stress. In addition, deviations from ideal clamping at the beam endpoints may also effect the mode shapes. Finally, however, it should be noted that the agreement between theory and experiment in Fig. 2(a) depends on the mode shapes being identical and so it is unlikely that the observed discrepancy in Fig. 2(b) can be explained fully through mode shape differences.

Using Eqs. (5a) and (5b), the measured spring constant of each mode, and the measured frequency shifts, one can determine K_T. From the out-of-plane and in-plane Duffing slopes, we find $K_T^{ex} = 4.05 \times 10^{13}\mathrm{N/m^3}$ and $5.36 \times 10^{13}\mathrm{N/m^3}$, respectively. From the pulling of the in-plane mode by the out-of-plane mode, we find $K_T^{ex} = 5.29 \times 10^{13}\mathrm{N/m^3}$, while the pulling of the out-of-plane mode by the in-plane mode gives $2.13 \times 10^{14}\mathrm{N/m^3}$. An analytical expression for K_T is given in the appendix and gives the theoretical value $K_T^{th} = 2.6 \times 10^{14}\,\mathrm{N/m^3}$, ~1.2 to 6.4 times higher than our experimental values.

B. Linear coupling

We then examined the linear coupling by measuring the resonance frequencies of the two modes, while increasing the DC gate bias. Fig. 3 shows the result of such a measurement using magnetomotive detection to measure the resonances. Note that while the sample was mounted with the in-plane mode approximately parallel to the magnetic field, a sight misalignment allowed us to detect the in-plane mode even at zero bias. As expected from the signs of the second derivatives of capacitance with respect to x and y, the in-plane (out-of-plane) resonance frequency decreases (increases) as the gate voltage increases. As the modes approach degeneracy, there is a clear avoidance observed.

The avoidance is consistent with a linear coupling.[7,8,12] Because the spectrum did not change as we lowered the drive power, and because the same spectrum was found using two very different detection methods, we again rule out parametric oscillations or other nonlinear effects.

For small amplitudes near degeneracy, we may neglect the nonlinear terms in Eq. (4). It will be convenient to put

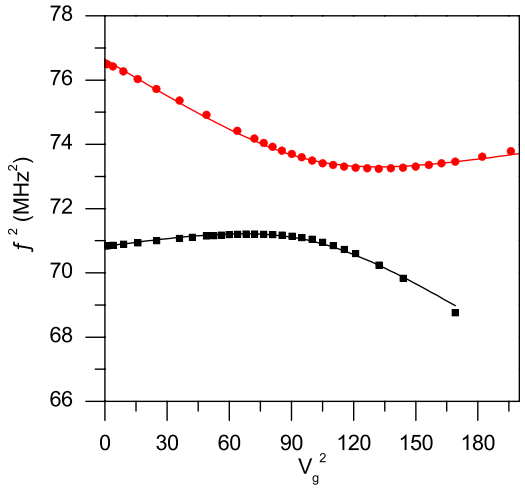

FIG. 3. Square of normal mode frequencies versus square of gate bias. Measurements made magnetomotively using $B \simeq 1.5$ T. Solid lines are least-squares fits to the predicted eigenfrequencies of the two coupled modes of the NEMS resonator, assuming that each mode frequency includes an electrostatic energy term proportional to the square of gate voltage, V_g^2, and that the linear coupling between the two modes is also proportional to V_g^2.

the coupled equations describing the amplitudes on resonance in matrix form

$$\begin{pmatrix} -M\omega^2 + K_x + \dfrac{iM\omega\omega_x}{Q_x} & K_{xy} \\ K_{xy} & -M\omega^2 + K_y + \dfrac{iM\omega\omega_y}{Q_y} \end{pmatrix} \begin{pmatrix} X_0 \\ Y_0 \end{pmatrix} = \begin{pmatrix} F_x \\ F_y \end{pmatrix}. \tag{6}$$

Assuming negligible damping and solving for the eigenfrequencies gives

$$\omega_{\mathrm{hi,lo}} = \frac{1}{\sqrt{2M}}\left[K_x + K_y \pm \sqrt{(K_x - K_y)^2 + 4K_{xy}^2}\right]^{\frac{1}{2}}, \tag{7}$$

where $\omega_{\mathrm{hi,lo}}$ refers to the upper and lower branches in Fig. 3. Here, K_x is the uncoupled in-plane spring constant including the electrostatic softening and K_y is the out-of-plane spring constant including the electrostatic stiffening, both of which are proportional to V_g^2 as per Eq. (3). ω_x and ω_y are the corresponding uncoupled natural frequencies of the two modes.

To test a purely electrostatic coupling model, we fit the data in Fig. 3 with a five-parameter nonlinear least squares curve fit to Eq. (7), including a voltage-dependent coupling parameter $K_{xy} = \alpha V_g^2$. Additional measurements were made over the course of 8 months, with cycles to room temperature in between each measurement that shifted the zero bias resonance frequencies of the two modes. In all cases, the fit yields a reduced χ^2 value better than 0.04. Fit parameters appear as the first five columns in Table I. The voltage dependence of spring constants K_x and K_y may be determined from the fit parameters $d(f_x^2)/d(V^2)$ and $d(f_y^2)/d(V^2)$. The intersection point (last column of Table I) indicates the voltage at which the uncoupled modes would be degenerate in the absence of a linear coupling.

TABLE I. Fitting parameters assuming voltage dependent coupling.

$f_{0,x}^2$	$f_{0,y}^2$	$\frac{d(f_x^2)}{d(V^2)}$	$\frac{d(f_y^2)}{d(V^2)}$	$\alpha/2\pi^2 M$	V_{degen}^2
MHz^2		(MHz/V)^2		(MHz/V)^2	V^2
76.65	70.82	0.0388	0.0090	0.02280	121.9
68.36	65.52	0.0444	0.0035	0.05040	59.4
68.12	64.77	0.0444	0.0056	0.04336	67.0
68.38	63.99	0.0452	0.0086	0.03507	82.1
67.13	64.20	0.0505	0.0084	0.04231	49.8

Near degeneracy the modes are no longer purely in-plane or purely out-of-plane, but rather a superposition of the two. The coupling should thus also lead to coupled amplitudes and quality factors. Including the driving force in the equations of motion, we can solve for normal mode amplitudes projected onto the in-plane and out-of-plane directions. For instance, the motion projected onto the out-of-plane direction is given by

$$Y_0(\omega) = \frac{\dfrac{F_y}{M}\left(\omega_x^2 - \omega^2 + \dfrac{i\omega\omega_x}{Q_x}\right) - \dfrac{K_{xy}F_x}{M^2}}{\left(\omega_x^2 - \omega^2 + \dfrac{i\omega\omega_x}{Q_x}\right)\left(\omega_y^2 - \omega^2 + \dfrac{i\omega\omega_y}{Q_y}\right) - \left(\dfrac{K_{xy}}{M}\right)^2} \tag{8}$$

with $\omega = \omega_{\mathrm{hi,lo}}$. An identical expression, with x and y transposed, gives $X_0(\omega)$, the amplitude projected onto the in-plane direction. In our initial measurements, the magnetomotive detection is strongly sensitive only to out-of-plane motion. Measured amplitudes vs. gate bias, along with results from Eq. (8) (normalized to match the measured values at low bias) are plotted in Fig. 4(a). We interpret this data in light of the above model: at voltages far below degeneracy, the lower frequency mode is comprised of out-of-plane motion and the higher frequency mode is in-plane motion; as the modes couple near degeneracy, both modes become a superposition of oscillations in both directions; at degeneracy, the modes project equally onto the external field; and for voltages far above the degeneracy point, the mode polarizations are reversed, with the high frequency mode now comprising out-of-plane motion, and the low frequency mode being in-plane motion. This rotation behavior of normal mode angles for the three voltage ranges is indicated by the diagrams above the plot. The discrepancy between data and model for the low frequency mode at high bias can be attributed to a loading effect described later in this article.

To experimentally determine the relative phase between the two modes and whether they remain orthogonal through degeneracy or go through a "whirling" motion, we tilted the sample $\Phi = 45^\circ$ relative to the magnetic field and repeated the amplitude vs. gate bias measurements. Fig. 4(b) shows the results. Since the magnetomotive amplitude depends on the mode's projection onto the magnetic field, a magnetic field at this angle will drive and detect both in-plane and out-of-plane motion equally. Driving the mode at ω_{hi} will detect an amplitude proportional to $|X_0(\omega_{\mathrm{hi}})\sin(\Phi) + Y_0(\omega_{\mathrm{hi}})\cos(\Phi)|$, while the measured amplitude of the ω_{lo} mode will be proportional to $|X_0(\omega_{\mathrm{lo}})\sin(\Phi) + Y_0(\omega_{\mathrm{lo}})\cos(\Phi)|$. When the two modes mix near degeneracy, the low frequency mode vanishes,

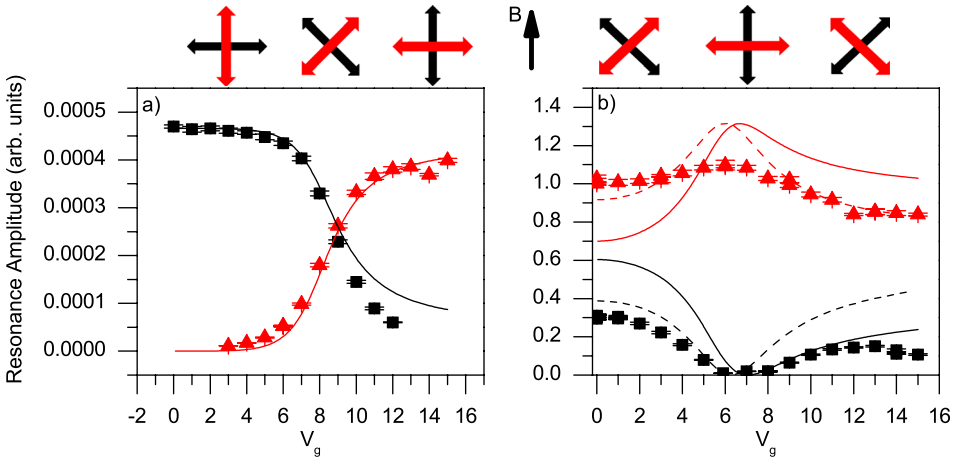

FIG. 4. Amplitude vs. gate bias of high frequency (triangles) and low frequency (squares) modes. Diagrams above graphs show orientation of modes relative to external field as gate bias is increased. (a) Sample oriented with in-plane mode parallel to applied $B = 1.5$ T field. Solid lines are the predicted behavior, assuming a voltage dependent mode coupling, scaled to match the zero bias data. (b) Sample oriented with in-plane and out-of-plane modes 45° to $B = 1$ T field. Solid lines are the predicted behavior with modes at 45° (solid) and 55° (dashed) to the field.

indicating that its physical angle is parallel to the B field and rotated 45° relative to the uncoupled modes. At the same point, the high frequency mode reaches a maximum, indicating that the modes remain perpendicular and linearly polarized but rotate their planes of polarization as they pass the degeneracy point. Also shown in Fig. 4(b) is the prediction of Eq. (8). (All prediction curves are scaled using a single scaling factor, to match the measured amplitudes over as much of the voltage range as possible.) We note improved agreement between theory and experiment if we assume $\Phi = 55^\circ$, rather than $\Phi = 45^\circ$. Such a deviation of 10° is the maximum angular error we expect in our apparatus.

Retaining the damping term in Eq. (6), the imaginary solutions to the resulting characteristic equation are equal to the half-width at half maximum for the two modes, or $\omega/2Q$. In Fig. 5, we plot normalized quality factors vs gate bias along with results from the model (normalized to match the measured quality factor at zero bias). At high bias, the high frequency mode's quality factor reduces to that of the low frequency mode at zero bias, as expected. In the low frequency mode, however, the measured quality factor does not reach the zero bias value of the high frequency mode, but rather drops far

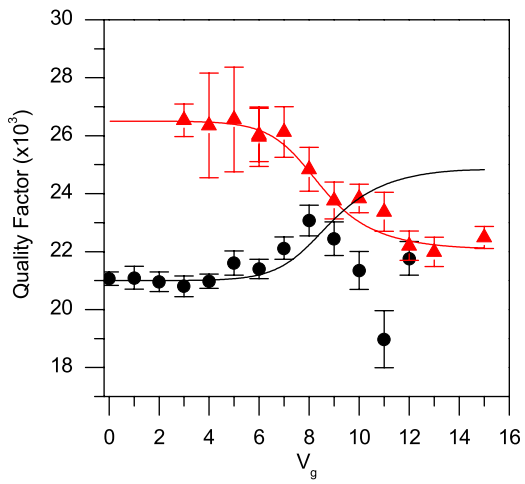

FIG. 5. Quality factors of high frequency (triangles) and low frequency (circles) modes vs gate voltage. Sample oriented with in-plane mode parallel to applied $B = 1.5$ T field. Solid lines are the predicted behavior, assuming a voltage-dependent mode coupling. Prediction does not include the effect of loading of the resonator by the capacitive detection circuit.

below it. This deviation is probably due to loading of the in-plane motion by the tank circuit[29] and 50 Ω external circuitry shown in Fig. 1. At high bias voltages, the low frequency mode comprises primarily in-plane motion and will be increasingly affected by such loading, reducing its quality factor below its unloaded value Q. We may estimate the loading as follows: the beam-gate system is modeled as a series LRC network comprising equivalent electromechanical impedances L_m, R_m, and C_m.[22] In parallel to the electromechanical impedance is the matching network comprising L_t, C_t, and R_t plus the 50 Ω cabling and amplifier (Fig. 1), exhibiting a quality factor $Q_t = \sqrt{\frac{L_t}{C_t}}/(R_t + 50)$. Inserting the tank circuit parameters given in Fig. 1, we find $Q_t = 20$. Solving the complex impedance of this combined network for its resonant frequencies and retaining the imaginary term as $\omega/2Q_L$, we find an approximate expression for the loaded quality factor Q_L, assuming that the mechanical and tank resonances are degenerate

$$Q_L \approx \frac{Q}{1 + \frac{R_t + 50}{R_m} Q_t^2}. \tag{9}$$

For $R_m = \frac{d^2 M \omega}{V_g^2 C_{bg}^2 Q}$ with $d = 165$ nm being the beam-gate distance, it is clear that Q_L falls with increasing V_g. At $V_g = 12$ V, we find that $Q_L/Q \approx 0.8$. This amount of loading is consistent with the reduction in quality factor evident in Fig. 5.

To examine whether the electrostatic coupling model can fully account for the observations, it is useful to look at the derivatives of capacitance in Eq. (3). To this end, we constructed a 2-dimensional finite element model using FEMLAB software. We modeled a cross-section of the beam-gate system to match the device dimensions in Fig. 1, using known dielectric constants of silicon and silicon nitride. On the underside of the beam, we assumed a residual ridge of silicon 100 nm thick. Using this model, we calculated the capacitance per unit length C of the metallized beam relative to the nearby gate. We neglected capacitance edge effects in the z dimension, treating C as constant over the length of the gate (i.e., for $|z| < \ell_g/2$) and zero elsewhere. We displaced the beam position in successive steps of 5 nm forward and backward in the in-plane and out-of-plane directions to find C as a function of x and y, and fit this dependency to a 2nd-order polynomial. The fit values yield $\partial^2 C(z)/\partial x^2 = 535\,\mathrm{F/m^3}$ and $\partial^2 C(z)/\partial y^2 = -128\,\mathrm{F/m^3}$.

TABLE II. Fitting parameters assuming voltage independent coupling.

$f_{0,x}^2$	$f_{0,y}^2$	$\frac{d(f_x^2)}{d(V^2)}$	$\frac{d(f_y^2)}{d(V^2)}$	$\beta/2\pi^2 M$	V_{degen}^2
MHz^2		$(MHz/V)^2$		MHz^2	V^2
76.36	71.11	0.0414	0.0116	2.52	99.2
67.92	65.96	0.0552	0.0143	2.06	28.2
67.71	65.18	0.0525	0.0137	2.19	38.2
68.02	64.35	0.0504	0.0136	2.41	57.4
66.86	64.48	0.0573	0.0152	1.71	32.9

Assuming a resonator mass of 1.3×10^{-15} kg, these predict frequency shifts of $d(f_x^2)/d(V^2) = 0.0820\,(\mathrm{MHz/V})^2$ and $d(f_y^2)/d(V^2) = 0.0196\,(\mathrm{MHz/V})^2$. These values are greater by about a factor of two than those found by the fit and given in Table I. The model also finds $\partial^2 C(z)/\partial x \partial y = 11\,\mathrm{F/m^3}$. This value predicts (see appendix) a mode coupling of $3.3 \times 10^{-3}(\mathrm{MHz/V})^2$, about an order of magnitude smaller than the experimental fit values for a voltage dependent coupling. Thus, at this point, we cannot rule out the majority of the coupling being due to some other effect besides the electrostatics.

For comparison, we also fit the frequency vs gate bias data with a voltage independent (fixed) coupling parameter, $K_{xy} = \beta$, and found that it was also able to fit the frequency vs bias data in Fig. 3 as well as the voltage dependent coupling model. The adjusted R-squared value for the data presented in Fig. 3 is 0.99913 for both fits. The resulting fit parameters for the different trials assuming voltage independent coupling are given in Table II.

IV. CONCLUSION

We have measured both the elastic nonlinear coupling as well as a linear coupling between the two fundamental transverse modes of a nanomechanical resonator. Combining these terms, we derive the following Hamiltonian for a system of two fundamental transverse modes of a doubly clamped beam

$$H = \frac{1}{2M}(P_x^2 + P_y^2) + \frac{1}{2}(K_x X^2 + K_y Y^2) + \frac{1}{4}K_T(X^4 + Y^4 + 2X^2Y^2) + K_{xy}XY, \quad (10)$$

where P_x and P_y are the generalized momenta of the two modes.

Magnetomotive measurements at different angles to the applied field indicate that the linearly coupled modes stay linearly polarized, while rotating their plane of polarization about the beam axis, which could be useful in applications, where one would like to control the spatial motion of a resonator using a single gate. With a sequence of gate voltage pulses, one should be able to move energy rapidly between one polarization and the other.

While others have observed mechanical mode coupling and identified electrostatic coupling as a likely mechanism,[12,30] to the best of our knowledge, no one has demonstrated a calculation of the capacitance derivatives modeled from the device geometry that reproduces the magnitude of the observed linear coupling. Indeed, while an electrostatic coupling is based on well-established theory and must be present, our capacitance model seems to indicate that it is a small contribution to the overall coupling. One possibility is that field gradients in the direction of the resonator's long axis, which are not accounted for in our 2D model, are the dominant source of coupling. In this case, careful shaping of the gate electrode may provide a mechanism for tuning the coupling to a desired strength. Another possibility is that the electrostatic coupling is a small correction to a much larger voltage independent coupling, perhaps an elastic coupling through the resonator supports. An alternative method to tune the resonator modes into degeneracy that does not rely on the gate voltage would be helpful in determining the nature of the coupling.

APPENDIX: DERIVATION OF EQUATIONS OF MOTION FOR TRANSVERSE MODES

Equations (4a) and (4b) are the coupled equations of motion for the two transverse modes, where X and Y represent the mode amplitudes. Here, we derive the in-plane (X) equation. The out-of-plane (Y) equation can be found in a similar manner.

We start with the Euler-Bernoulli equation for the free vibration of an undamped beam. With the long axis of the beam along the z direction, the displacement profile of the beam in the plane of the substrate, $x(z, t)$, satisfies the wave equation

$$\frac{m}{\ell}\frac{\partial^2 x}{\partial t^2} + EI_x\frac{\partial^4 x}{\partial z^4} = 0, \quad (A1)$$

where m/ℓ is the mass per unit length, E is the Young's modulus, and I_x is the in-plane area moment of inertia, all constant over the length of the beam. This equation can be solved by separation of variables

$$x_n(z,t) = X_n(t)u_n(z), \quad (A2)$$

where X is the amplitude and $u_n(z)$ is the mode shape of the n^{th} normal mode, given by

$$u_n(z) = N_n\left[\cosh(\eta_n)\cos\left(\frac{2\eta_n z}{\ell}\right) - \cos(\eta_n)\cosh\left(\frac{2\eta_n z}{\ell}\right)\right]. \quad (A3)$$

We are only interested in the lowest ($n = 1$) vibrational mode, so we will leave off the subscript n from here on. For this mode, $\eta \simeq 2.365$. We determine the normalization constant, N_1, by setting the integral of the mode shape equal to the length of the beam

$$\int_{-\ell/2}^{\ell/2} u(z)\mathrm{d}z = \ell. \quad (A4)$$

This choice of normalization gives $N \simeq 3.1821^{-1}$, and defines $X(t)$ as the average displacement of the beam, which is apparent

$$X_{avg} = \frac{X}{\ell}\int_{-\ell/2}^{\ell/2} u(z)\mathrm{d}z. \tag{A5}$$

We now include the displacement dependent tension given in Eq. (1), a velocity dependent damping term, and the electrostatic force given in Eq. (3), along with a driving force

$$\frac{m}{\ell}\frac{\partial^2 x}{\partial t^2} + \mu_{\mathrm{x}}\frac{\partial x}{\partial t} + EI_{\mathrm{x}}\frac{\partial^4 x}{\partial z^4} - \frac{V_{\mathrm{g}}^2}{2}\frac{\partial^2 C}{\partial x^2}x - \frac{V_{\mathrm{g}}^2}{2}\frac{\partial^2 C}{\partial x \partial y}y - T(x,y)\frac{\partial^2 x}{\partial z^2} = f_D(z,t), \tag{A6}$$

where $\mu_{\mathrm{x}} = (m/\ell)\omega_{0,x}/Q$ and C are the dissipation and capacitance per unit length, respectively, and V_g is the gate voltage. We treat the derivatives of the capacitance as constant in time and in z over the length, ℓ_g, of the gate electrode and zero elsewhere, so that the total beam-gate capacitance is $C_{bg} = \ell_g C$. We omit the first term in Eq. (3), which serves only to shift the beam's equilibrium position. In principle, this static deflection, $X_s \sim V_g^2 C'/K_x$, produces additional linear and nonlinear terms through added tension. Readers wishing to learn more about the effect of these terms, particularly on the dynamic range, are encouraged to see Ref. 23. In our case, the nonlinear measurements represented in Fig. 2 were performed at a low gate voltage, where the additional voltage dependent nonlinear terms are insignificant, while our voltage dependent measurements were performed at a low drive amplitude so that the beam was in the linear regime. At the highest gate voltage used (15 V), we find that $X_s < 30\,\mathrm{nm}$. Even with this large a shift in equilibrium position, however, we find the contribution to the spring constant due to static deflection to be about 20 times smaller than the contribution from the second order capacitance derivatives.

Equation (A6) is a nonlinear differential equation that must be solved numerically. Instead, we approximate a solution by assuming that the dissipation, tension, and electrostatic and driving forces are small enough that the mode shape remains approximately that given in Eq. (A3). Substituting Eq. (A2) with this mode shape into Eq. (A6), multiplying both sides by $u(z)$, and integrating over the length of the beam, we get an equation for the time dependence of the beam's motion

$$M\left(\frac{\mathrm{d}^2 X}{\mathrm{d}t^2} + \frac{\omega_{0,\mathrm{x}}}{Q_{\mathrm{x}}}\frac{\mathrm{d}X}{\mathrm{d}t}\right) + K_{\mathrm{x}}X + K_{\mathrm{xy}}Y + K_T(X^3 + Y^2X) = F_{\mathrm{x}}. \tag{A7}$$

In the last term, the amplitude of the out-of-plane mode, Y, enters through the tension (see Eq. (1)). F_{x} is the product of the mode shape $u(z)$ with the driving force f_D, integrated over the length of the beam.

The coefficients in (A7) are given by

$$M = \frac{m}{\ell}\int_{-\ell/2}^{\ell/2} u^2(z)\mathrm{d}z \simeq 1.45\,m, \tag{A8}$$

$$K_{\mathrm{x}} = EI_{\mathrm{x}}\left(\frac{2\eta}{\ell}\right)^4\int_{-\ell/2}^{\ell/2} u^2(z)\mathrm{d}z - \frac{V_{\mathrm{g}}^2}{2}\frac{\partial^2 C}{\partial x^2}\int_{-\ell_g/2}^{\ell_g/2} u^2(z)\mathrm{d}z \simeq 725.08\frac{EI_{\mathrm{x}}}{\ell^3} - 1.36\ell\frac{V_{\mathrm{g}}^2}{2}\frac{\partial^2 C}{\partial x^2}, \tag{A9}$$

$$K_{\mathrm{xy}} = -\frac{V_{\mathrm{g}}^2}{2}\frac{\partial^2 C}{\partial x \partial y}\int_{-\ell_g/2}^{\ell_g/2} u^2(z)\mathrm{d}z \simeq -1.36\ell\frac{V_{\mathrm{g}}^2}{2}\frac{\partial^2 C}{\partial x \partial y}, \tag{A10}$$

$$K_T = \frac{AE}{2\ell}\left[\int_{-\ell/2}^{\ell/2}\left(\frac{\mathrm{d}u(z)}{\mathrm{d}z}\right)^2\mathrm{d}z\right]^2 \simeq 158.8\frac{AE}{\ell^3}, \tag{A11}$$

[1] K. L. Ekinci, X. M. H. Huang, and M. L. Roukes, Appl. Phys. Lett. **84**, 4469 (2004).
[2] B. Ilic, Y. Yang, and H. G. Cragihead, Appl. Phys. Lett. **85**, 2604 (2004).
[3] J. A. Sidles, J. L. Garbini, K. J. Brulad, D. Rugar, O. Zuger, S. Hoen, and C. S. Yannoni, Rev. Mod. Phys. **67**, 249 (1995).
[4] D. Rugar, R. Budakian, H. J. Mamin, and B. W. Chui, Nature **430**, 329 (2004).
[5] J. W. Baldwin, M. K. Zalalutdinov, T. Feygelson, B. B. Pate, J. E. Butler, and B. H. Houston, Diamond Relat. Mater. **15**, 2061 (2006).
[6] A. Erbe, H. Krümmer, A. Kraus, R. H. Blick, G. Corso, and K. Richter, Appl. Phys. Lett. **77**, 3102 (2000).
[7] G. Anetsberger, R. Rivière, A. Schliesser, O. Arcizet, and T. J. Kippenberg, Nature Photon. **2**, 627 (2008).
[8] C. Chen, S. Rosenblatt, K. I. Bolotin, W. Kalb, P. Kim, I. Kymissis, H. L. Stormer, T. F. Heinz, and J. Hone, Nat. Nanotechnol. **4**, 861 (2009).
[9] D. Antonio, D. H. Zanette, and D. López, Nat. Commun. **3**, 806 (2011).
[10] K. J. Lulla, R. B. Cousins, A. Venkatesan, M. J. Patton, A. D. Armour, C. J. Mellor, and J. R. Owers-Bradley, New J. Phys. **14**, 113040 (2012).
[11] A. Castellanos-Gomez, H. B. Meewaldt, W. J. Venstra, H. S. J. van der Zant, and G. A. Steele, Phys. Rev. B **86**, 041402 (2012).
[12] T. Faust, J. Rieger, M. J. Seitner, P. Krenn, J. P. Kotthaus, and E. M. Weig, Phys. Rev. Lett. **109**, 037205 (2012).
[13] R. B. Karabalin, M. C. Cross, and M. L. Roukes, Phys. Rev. B **79**, 165309 (2009).
[14] W. J. Venstra, H. J. R. Westra, and H. S. J. van der Zant, Appl. Phys. Lett. **99**, 151904 (2011).
[15] D. H. Santamore, A. C. Doherty, and M. C. Cross, Phys. Rev. B **70**, 144301 (2004).
[16] D. H. Santamore, H. S. Goan, G. J. Milburn, and M. L. Roukes, Phys. Rev. A **70**, 052105 (2004).
[17] N. Imoto, H. A. Haus, and Y. Yamamoto, Phys. Rev. A **32**, 2287 (1985).
[18] B. Yurke, D. S. Greywall, A. N. Pargellis, and P. A. Busch, Phys. Rev. A **51**, 4211 (1995).
[19] M. Spletzer, A. Raman, A. Q. Wu, X. Xu, and R. Reifenberger, Appl. Phys. Lett. **88**, 254102 (2006).
[20] R. B. Karabalin, R. Lifshitz, M. C. Cross, M. H. Matheny, S. C. Masmanidis, and M. L. Roukes, Phys. Rev. Lett. **106**, 094102 (2011).
[21] M. C. Cross, J. L. Rogers, R. Lifshitz, and A. Zumdieck, Phys. Rev. E **73**, 036205 (2006).
[22] P. A. Truitt, J. B. Hertzberg, C. C. Huang, K. L. Ekinci, and K. C. Schwab, Nano Lett. **7**, 120 (2007).
[23] I. Kozinsky, H. W. C. Postma, I. Bargatin, and M. L. Roukes, Appl. Phys. Lett. **88**, 253101 (2006).
[24] Y. T. Yang, K. L. Ekinci, X. M. H. Huang, L. M. Schiavone, and M. L. Roukes, Appl. Phys. Lett. **78**, 162 (2001).
[25] L. Jiang, R. Cheung, R. Brown, and A. Mount, J. Appl. Phys. **93**, 1376 (2003).
[26] L. Jiang, R. Cheung, M. Hassan, A. J. Harris, J. S. Burdess, C. A. Zorman, and M. Mehregany, J. Vac. Sci. Technol. B **21**, 2998 (2003).
[27] A. N. Cleland and M. L. Roukes, Sens. Actuators A **72**, 256 (1999).
[28] R. E. Mickens, *An Introduction to Nonlinear Oscillations* (Cambridge University Press, New York, 1981).
[29] In our configuration, the RF drive is applied near the resonance frequency of the tank circuit, which is tuned to be at the same frequency as the mechanics, and so we ignore optomechanical type effects on the frequency and damping of the resonator in our analysis.
[30] H. S. Solanki, S. Sengupta, S. Dhara, V. Singh, S. Patil, R. Dhall, J. Parpia, A. Bhattacharya, and M. M. Deshmukh, Phys. Rev. B **81**, 115459 (2010).